American Mineralogist, Volume 108, pages 2121–2130, 2023

Amorphous Mn_2SiO_4: A potential manganese phase in the stagnant slab

Zhilin Ye[1,2], Jingui Xu[1,3,*], Dawei Fan[1,*], Dongzhou Zhang[3,†], Wenge Zhou[1], and Hongsen Xie[1]

[1]Key Laboratory of High-Temperature and High-Pressure Study of the Earth's Interior, Institute of Geochemistry, Chinese Academy of Sciences, Guiyang, Guizhou 550081, China
[2]University of Chinese Academy of Sciences, Beijing 100049, China
[3]Hawaii Institute of Geophysics and Planetology, School of Ocean and Earth Science and Technology, University of Hawaii at Manoa, Honolulu, Hawaii 96822, U.S.A.

Abstract

Tephroite (Mn_2SiO_4), together with some manganese (Mn)-rich mineral inclusions, has been found in ophiolite-hosted diamonds, possibly originating from Mn-nodules and sediments that were once deposited on the oceanic floor and later subducted into the deep mantle, which provides evidence for oceanic crustal recycling. However, the state and behavior of tephroite under high-pressure and high-temperature conditions remain poorly understood. In this study, we conducted in situ synchrotron single-crystal X-ray diffraction (XRD) and Raman spectroscopy of synthetic tephroite up to ~30 GPa and ~900 K. The XRD and Raman spectroscopy experiments in this study first show that tephroite undergoes a pressure-induced, irreversible, amorphous transformation above ~20 GPa. Temperature (<900 K) is found to be an insignificant factor governing the process of amorphous transformation. Amorphous tephroite may be a potential phase in a rapidly cooling oceanic lithospheric subduction slab stagnating at the bottom of the mantle transition zone.

Keywords: Tephroite, amorphization, single-crystal X-ray diffraction, high-pressure Raman spectra, stagnant slab

Introduction

Olivine, the most dominant mineral in the Earth's mantle, is an important solid-solution silicate composed of end-member forsterite (Mg_2SiO_4) and fayalite (Fe_2SiO_4) (Ringwood 1991). It is also found in igneous and metamorphic rocks, meteorites, and many other extraterrestrial environments (Mason 1963; Nguyen and Zinner 2004; Mustard et al. 2005; Zolensky et al. 2006; Finkelstein et al. 2014). In addition, other end-member olivines composed of transition metal ions [e.g., tephroite (Mn_2SiO_4) and libenbergite (Ni_2SiO_4)] are found in nature. Even a small concentration of transition metals can profoundly influence the optical, magnetic, and transparency properties and thermodynamic behaviors of crystals (Geiger et al. 2019). The existence of transition metal elements also affects large-scale geodynamic processes such as redox reactions and deep mantle melting on Earth (Gaillard et al. 2015).

Recently, tephroite associated with other manganese (Mn)-rich minerals, such as spessartine (Mn garnet) (Ca,Mn)SiO_3-perovskite, MnO, and NiMnCo alloy, was discovered in ophiolite-hosted diamonds (Yang et al. 2015a, 2015b; Lian et al. 2018; Lian and Yang 2019), which has never been found in other diamonds. These significant ranges of ultrahigh-pressure (UHP) and highly reduced inclusions in ophiolite-hosted diamonds reflect a completely new environment for diamond formation in the mantle. It is suggested that these minerals may be a common feature of the in situ oceanic lithosphere (Yang et al. 2015b). Generally, Mn-rich olivine associated with iron-Mn ore deposits and skarns is formed by complex interactions in the ocean-atmosphere-lithosphere system (Cloutis 1997). However, research focused on the properties of tephroite under high-pressure and high-temperature conditions is limited. Isomorphic forsterite and fayalite both undergo different phase transitions at high pressure and high temperature. Mg_2SiO_4 transforms into wadsleyite (spinelloid structure) at 12–15 GPa and further into ringwoodite (spinel structure) at ~18–20 GPa (Frost 2008), while Fe_2SiO_4 transforms directly into a spinel structure at 6–7 GPa. Moreover, pressure-induced amorphizations (PIAs) of forsterite and fayalite are observed at room temperature and higher pressures of 56–80 GPa (Jeanloz et al. 1977; Guyot and Reynard 1992; Durben et al. 1993; Andrault et al. 1995; Rouquette et al. 2008; Santamaria-Perez et al. 2016; Kim et al. 2021) and ~35 GPa (Richard and Richet 1990; Williams et al. 1990; Andrault et al. 1995; Speziale et al. 2004), respectively. Recently, it has been proposed that amorphization takes place at the forsterite grain boundary under stress, which can trigger a plastic process in the deep Earth and greatly affect the transition layer of the lithospheric transition zone (Samae et al. 2021).

However, the only study that focused on the stability of tephroite indicates that tephroite does not undergo a transformation into either spinelloid or spinel structure like forsterite and fayalite but decomposes into MnO (rock salt) and $MnSiO_3$ (tetragonal garnet-like structure) at $P > 14$ GPa and $T = 1273$ K and at higher pressure ($P > 30$ GPa) into MnO and SiO_2 (Ito et al. 1974). Whether tephroite undergoes a similar phase transformation or amorphization in a high-temperature and high-pressure range like forsterite and fayalite and the impact of such a transformation are

* E-mail: fandawei@vip.gyig.ac.cn. Orcid 0000-0001-7840-2075 (D. Fan); xujingui@vip.gyig.ac.cn (J. Xu).
† Orcid 0000-0002-6679-892X

uncertain. Therefore, knowledge of the high-pressure and high-temperature behaviors of tephroite would help us to understand the occurrence of tephroite in the deep Earth and provide new insights into the process of its encapsulation in the diamond.

To address these issues, we investigated the stability of single-crystal tephroite through in situ synchrotron single-crystal X-ray diffraction (SCXRD) and Raman scattering experiments at high pressures and high temperatures, simulating conditions within the cold subducting lithosphere. The compressive equation of state, compression mechanism, thermal stability, and PIA of tephroite are determined up to ~30 GPa and ~900 K in this study. The results indicate that tephroite may be able to exist in the Earth's interior in an amorphous state and transform into crystalline phases on its way back to the surface by being wrapped in the diamond.

Methods

Sample preparation

The tephroite sample measured in this study was synthesized using high-purity oxides (MnO, SiO_2) in a multi-anvil high-pressure apparatus at 4.0 GPa and 1273 K for 36 h at the Institute of Geochemistry, Chinese Academy of Sciences, Guiyang, China. Electron microprobe analysis (EMPA) was carried out with an EMPA1600, operating at an acceleration voltage of 25 kV, beam current of 10 nA, and focused electron beam of ~5 μm, with which the chemical composition of the sample was determined to be $Mn_{1.98}Si_{0.98}O_4$ (Online Materials[1] Table S1).

In situ single-crystal X-ray diffraction

A 30 × 40 μm² fragment of single-crystal tephroite with a thickness of <15 μm was mounted on a polymer holder used for room-pressure measurement. The high-pressure experimental samples were loaded in a symmetric-type DAC with ±32° opening angles equipped with a pair of 300 μm culet-size diamond anvils, while the high-pressure and high-temperature experimental sample was loaded in a BX90 externally heated diamond-anvil cell (EHDAC) with ±15° opening angles equipped with a pair of 500 μm culet-size diamond anvils. A resistive heater was used to generate a maximum temperature of 900 K, and the temperature was measured by a K-type thermocouple. The temperature of the experiment was raised from room temperature to a maximum temperature of 900 K at intervals of 200 K and then cooled to room temperature at the same interval. After pressurization at room temperature, the same heating and cooling operation was conducted (Online Materials[1] Fig. S1). The pressure was determined by the calibrated shift of the R1 ruby fluorescence band (Mao et al. 1986) for the high-pressure experiments and the equation of state of gold (Fei et al. 2007) for the high-pressure and high-temperature experiments. Neon was used as the pressure-transmitting medium (Rivers et al. 2008).

The in situ synchrotron SCXRD experiments were conducted at experimental station 13-BM-C of the Advanced Photon Source at Argonne National Laboratory; experimental details were previously described (Xu et al. 2020b; Ye et al. 2021). The Bruker APEX3 software package was used to analyze the diffraction images, and crystal refinements were carried out with the SHELXL and Olex2 software packages (Sheldrick 2008; Dolomanov et al. 2009), starting from the *Pbnm* structure modeled by Fujino et al. (1981) to initialize the refinement. All atoms in this study were modeled with isotropic atomic displacement parameters (U_{iso}). The crystal structure of tephroite under ambient conditions is diagramed in Online Materials[1] Figure S2 by the VESTA program (Momma and Izumi 2011). The unit-cell parameters are shown in Online Materials[1] Table S2, and the refinement details can be seen in Online Materials[1] Tables S3 and S4.

Raman spectroscopy

High-pressure Raman spectra were collected between 37–1300 cm^{-1} using a Renishaw RM 1000 Raman microscope with a Peltier-cooled charge-coupled device (CCD) detector at the Center for High Pressure Science and Technology Advanced Research. Raman spectra were obtained using a 532 nm wavelength from the Ar^+ laser with a maximum spot of ~2 μm. The sample was focused through a Nikon L Plan EPI 20X with a 0.35 objective. At each pressure step, the Raman spectrum was collected for a duration of 300 s. All spectra were obtained in the backscattering geometry with no polarization used for the collected signal. The Raman spectra were analyzed by Lorentzian curve fitting using the PeakFit program (Systat Software, San Jose, California, U.S.A.).

Results

PVT equation of state of tephroite

During continuous pressurization to 29.9(2) GPa in the room-temperature and high-pressure experiment, SCXRD shows that tephroite retains the initial *Pbnm* olivine structure up to ~20 GPa (Online Materials[1] Table S1 and Fig. S1). As shown in Figure 1, the SCXRD images reflect a phase transformation of tephroite characterized by conspicuous changes after ~20 GPa. The SCXRD images after phase transformation exhibit fewer peaks than those of the initial tephroite phase. The loss of sharp crystalline diffraction peaks indicates that tephroite undergoes PIA. This is the first time that tephroite has been observed to undergo amorphous transformation. Due to the occurrence of amorphization, unit-cell parameters and structural information of tephroite above 20 GPa cannot be obtained.

The *P-V* compression curve of the tephroite sample in the pressure range of 0–20 GPa was fitted to the third-order Birch-Murnagham equation of state (BM3-EoS) (Birch 1947) using the EoSFit software package (Angel et al. 2014). The EoS parameters, including the zero-pressure volume (V_{T0}), isothermal bulk modulus (K_{T0}), and its pressure derivative (K'_{T0}), were obtained without any constraints. The best-fit parameters are: V_{T0} = 325.22(13) Å, K_{T0} = 124(1) GPa, and K'_{T0} = 4.67(29). Compared with other end-member olivines, the bulk modulus of tephroite indicates that it is the most compressible end-member studied (Online Materials[1] Table S5). The bulk modulus of transition-metal olivine $(Mn,Fe,Co,Ni)_2SiO_4$ decreases linearly with increasing ionic radius (Online Materials[1] Fig. S3). The relationship between the Eulerian strain (f_E) and normalized pressure (F_E) shows a slightly positive slope (Fig. 2a). The weighted linear fit of the f_E-F_E plot yields K_{T0} [124.3(8) GPa] and $K'_{T0} > 4$, which are in good agreement with those from the BM3-EoS fit, indicating that the BM3-EoS is suitable for fitting the high-pressure data. The axial compressibilities are also determined using the BM3-EoS (Online Materials[1] Fig. S4 and Table S6). The ambient-pressure axial compressibility β_{l0} is defined as $1/(3M_{l0})$. At ambient pressure, the axial compressibilities of the three axes are $\beta_{a0} = 6.03(16) \times 10^{-4}$ GPa^{-1}, $\beta_{b0} = 1.22(2) \times 10^{-3}$ GPa^{-1}, and $\beta_{c0} = 9.78(37) \times 10^{-4}$ GPa^{-1}. The ratio of the axial compressibility at ambient pressure is $\beta_{a0}:\beta_{b0}:\beta_{c0}$ = 1.00:2.02:1.62. The tephroite crystal exhibits elastic anisotropy under compression, where the compressibility along the *b*-axis is the highest. The relative axial compressibility of tephroite is comparable to that of other end-member olivines (Online Materials[1] Fig. S4). To accurately account for the further understanding of compressional behavior under high pressure, we investigate polyhedral compression with pressure by crystal structure refinement. The pressure dependencies of polyhedral volumes and averaged bond length are shown in Online Materials[1] Figures S5a, S5b, and S6.

The high-pressure and high-temperature experiments yield the same results as the room-temperature and high-pressure experiments; that is, tephroite becomes amorphous upon pressurization to 20 GPa at a temperature of 900 K. After the amorphous transformation, tephroite does not return to its initial crystal structure despite a drop in temperature or pressure from the highest temperature and pressure in this study (~900 K and ~25.5 GPa). Similar to the

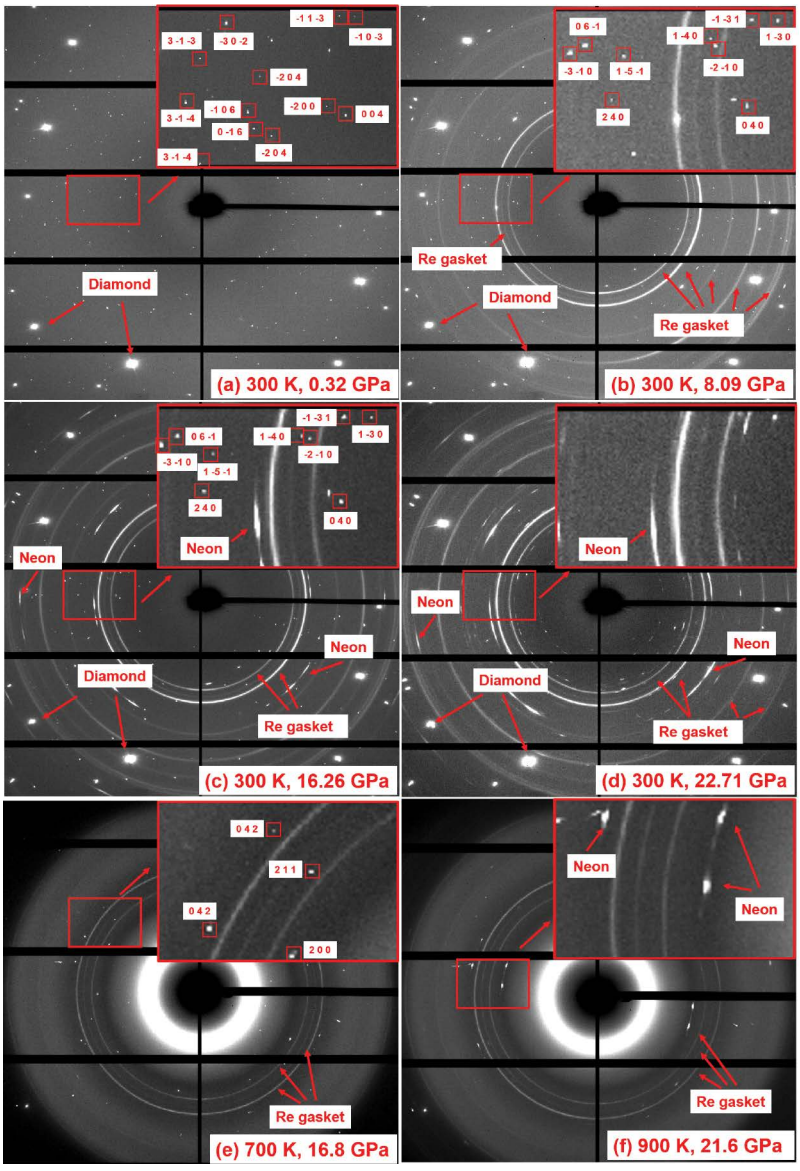

Figure 1. Single-crystal X-ray diffraction patterns of tephroite at different pressure and temperature conditions. The Miller indices of selected diffraction peaks are also shown for each phase at specific pressures. Sharp crystalline diffraction peaks appear after 20 GPa. All new closed rings are identified to Re gasket. (Color online.)

results of the room-temperature and high-pressure experiments, the pressure of the amorphous transformation of tephroite in the high-pressure and high-temperature experiments is ~20 GPa. Temperature does not have a conspicuous effect on the amorphous transformation.

The pressure-volume-temperature (*P-V-T*) data of tephroite below 20 GPa are fitted by the high-temperature third-order Birch-Murnaghan equation of state (HT-BM3-EoS) (Birch 1947; Fei 1995) using the EoSFit software package (Angel et al. 2014) (Fig. 2b). The obtained thermal EoS parameters are V_{T0} = 324.95(7) Å, K_{T0} = 122.5 GPa, K'_{T0} = 4.07(25), the temperature derivative of the bulk modulus $(\partial K_T/\partial T)_P$ is –0.022(3) GPa·K^{-1} and the thermal expansion at room pressure (α_0) is 4.20(17) × 10^{-5} K^{-1}.

Raman spectra of tephroite at high pressures

Olivine (M_2SiO_4, M = Mg, Fe, Mn, Ni, Co) is orthorhombic, belongs to space group D^{16}_{2h}, and contains four M_2SiO_4 formula units in its unit cell. The symmetry analysis of invariant atoms predicts 84 vibrational modes in the structure of olivine, of which the 36 Raman-active vibrational modes are $11A_g + 11B_{1g} + 7B_{2g} + 7B_{3g}$ (Chopelas 1991; Kolesov and Geiger 2004). The prominent two Raman peaks (ν_1 and ν_3) of olivine crystals are the Si-O stretching mode produced by the coupled vibration of the SiO_4 tetrahedron between 800 and 1000 cm^{-1} under ambient conditions.

The spectra of tephroite collected in this experiment are unpolarized (Fig. 3), which ensures that the major peaks can be

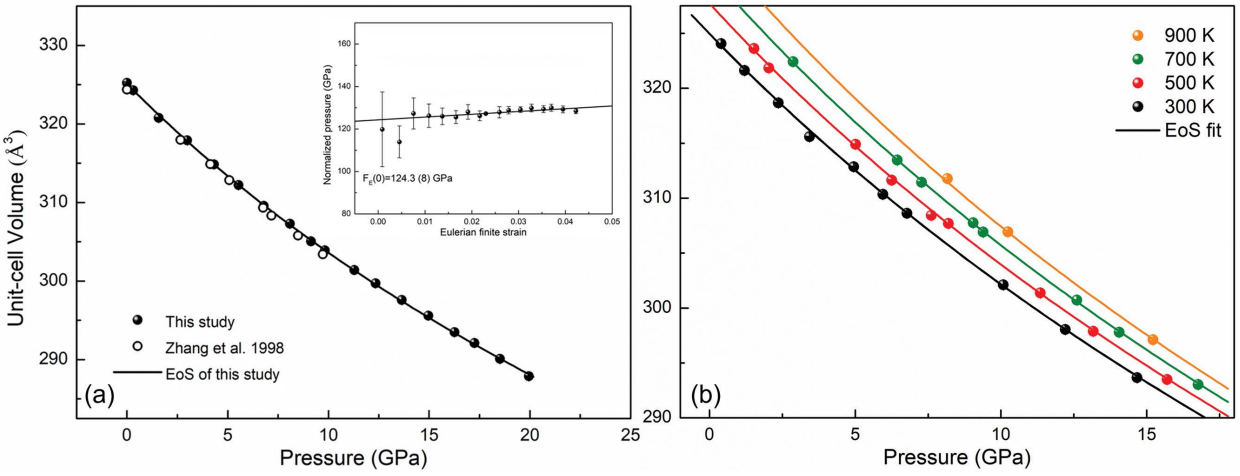

Figure 2. (**a**) Unit-cell volume compression curve of tephroite and the best-fit BM3 equation of state. Inset: Eulerian finite stain-normalized pressure (F_E–f_E) plot of tephroite. The solid lines represent the linear fit to the data. (**b**) Pressure-volume-temperature relationships of tephroite. The isothermal compression curves are calculated with the thermal EoS parameters obtained in this study. (Color online.)

represented and that the wavenumbers of individual bands can be determined by Lorentzian curve fitting (Online Materials[1] Table S7). However, some bands shown in the polarized single-crystal spectrum are not observed in the spectrum obtained under ambient conditions. Thirteen of the 36 Raman-active vibrational modes of tephroite observed are distributed as follows (Fig. 3): symmetric (ν_1) and asymmetric (ν_3) Si-O stretching modes of SiO_4^{4-} in the range of 810–935 cm^{-1}; symmetric (ν_2) and asymmetric (ν_4) O-Si-O bending modes between 392–515 cm^{-1}; and lattice vibrations involving translations of Mn^{2+} as well as translations and vibrations of SiO_4 tetrahedra in the range of 243–317 cm^{-1}.

The Raman spectra of a single-crystal sample of tephroite at high pressures are obtained by quasi-hydrostatic pressurization in a Ne pressure medium up to 29.1 GPa (Fig. 3). The Raman-active modes shift toward higher frequencies with increasing pressure. The vibrational frequency is linearly fitted to the pressure, and the slopes of $(\partial\nu_i/\partial P)_T$ (cm^{-1}/GPa) show that the frequencies increase at rates of 1.3–4.7 cm^{-1}/GPa under pressurization (Fig. 4). In the high-pressure experiment, the signal collected through the diamond windows becomes relatively weak, especially for lattice vibrations in the low-frequency range. The peaks at 276, 287, and 302 cm^{-1} gradually become undetectable as the pressure increases. The principal Raman peaks show slight peak broadening and intensity weakening at ~21.3 GPa, accompanied by the appearance of some new peaks at 244, 622, and 812 cm^{-1} and loss of definition in the high-frequency modes. However, upon decompression, the pressure-induced phase transformation of tephroite does not return to its initial structure. This phenomenon is consistent with the results obtained by the SCXRD experiment in this study; that is, tephroite undergoes a pressure-induced amorphous phase transition at ~20 GPa.

The isothermal-mode Grüneisen parameters (γ_{iT}) describe the variation in ν_i with pressure at a constant temperature according to the following formula (Gillet and Guyot 1988):

$$\gamma_{iT} = \left(\frac{\partial \ln \nu_i}{\partial \ln \rho}\right) = \frac{K_T}{\nu_{0i}}\left(\frac{\partial \nu_i}{\partial P}\right)_T \quad (1)$$

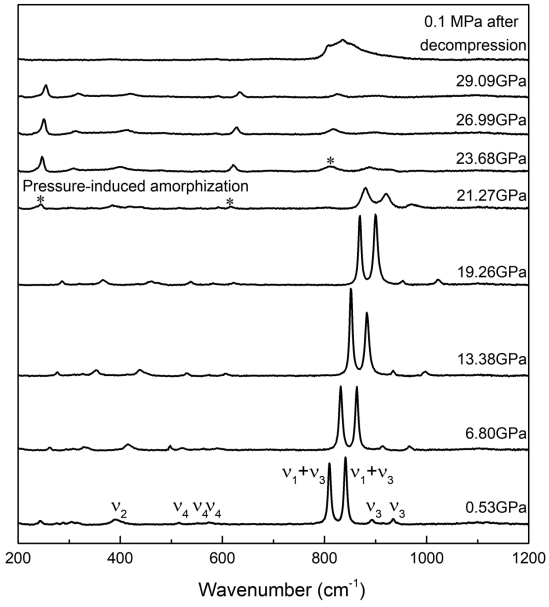

Figure 3. Representative room-temperature Raman scattering spectra of tephroite obtained in this study up to 29.09 GPa on the stroke and after decompression to 0.1 MPa. Asterisks (*) represent new peaks.

where ν_{0i} is the mode frequency under ambient conditions, ρ is the molar density, and K_T is the isothermal bulk modulus. The isothermal bulk modulus obtained for tephroite in this study is 124 GPa, and the calculated γ_{iT} mode Grüneisen parameters ranging from 0.3 to 1.64 are shown in Online Materials[1] Table S7.

Discussion

Compressional behavior of tephroite

The tephroite structure is described as an expanded and distorted hexagonally close-packed (hcp) array of O atoms. There are three polyhedral sites in the tephroite: $Mn1O_6$ octahedra, $Mn2O_6$ octahedra, and SiO_4 tetrahedra (Online Materials[1]

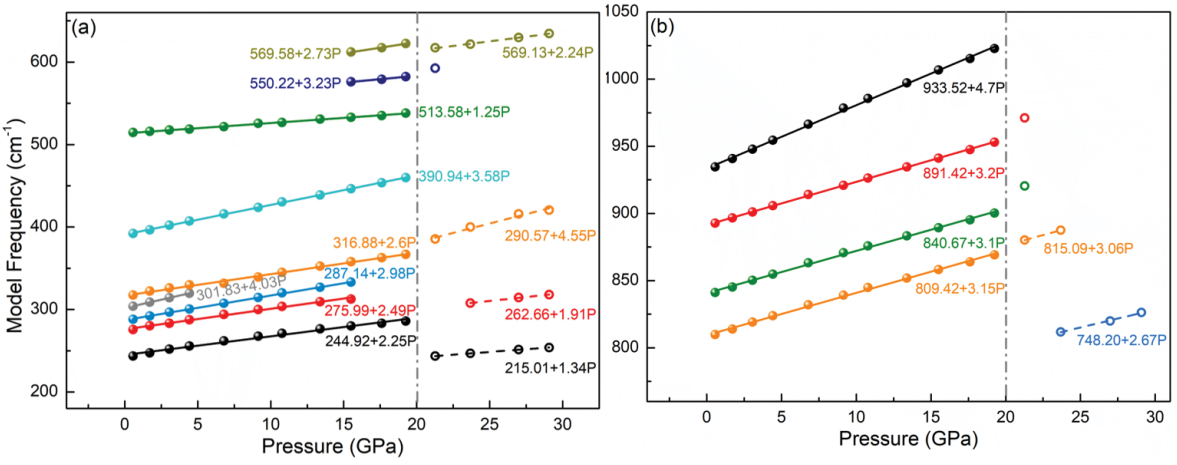

Figure 4. Pressure dependence of the Raman-active modes for tephroite in the frequency ranges of (**a**) 180–660 cm^{-1} and (**b**) 700–1050 cm^{-1}, with linear regression for each vibrational data set. (Color online.)

Fig. S2). The pressure dependencies of the polyhedral volumes and average bond length are shown in Online Materials[1] Figures S5a and S5b. The volumes of octahedral $Mn1O_6$ (–0.057 $Å^3$/GPa) and $Mn2O_6$ (–0.09 $Å^3$/GPa) and tetrahedral SiO_4 (–0.011 $Å^3$/GPa) are approximately linearly compressed with increasing pressure. This result reflects that the compressive behavior of tephroite is mainly controlled by the $Mn1O_6$ and $Mn2O_6$ polyhedra. The reduction in the Mn2-O average bond length (–4.1%) and $Mn2O_6$ polyhedral volume (–13.7%) is slightly larger than that of the Mn1-O average bond length (–2.8%) and $Mn1O_6$ polyhedron volume (–8.6%), so $Mn2O_6$ is more compressible than $Mn1O_6$ (Online Materials[1] Fig. S5). However, the average bond lengths of Mn1-O and Mn2-O are equal, as are the polyhedral volumes of $Mn1O_6$ and $Mn2O_6$, when the amorphization pressure of ~20 GPa is reached. In fayalite and libenbergite, there is no phenomenon of amorphization when the average bond length (Mn1-O and Mn2-O) and polyhedral volume ($Mn1O_6$ and $Mn2O_6$) are the same at ~15 and ~30 GPa, respectively (Zhang et al. 2017, 2019).

The degree of shortening of the Si-O bond is 3.2%, which is greater than that of Mn1-O by ~2.8%. For comparison, the average bond lengths of Si-O are shortened by only 1.4, 1.5, and 1.6% in forsterite, fayalite, and libenbergite, respectively (Zhang et al. 2017, 2019; Xu et al. 2020a), in the same pressure range of ~20 GPa. Due to the substitution of Mn^{2+} in olivine, the average bond lengths of Mn1-O and Mn2-O at 20 GPa cause a large change in that of Si-O, which may be a dominant factor influencing the PIA of tephroite under relatively low pressure compared with other olivines.

Pressure effect on Raman spectra and vibrational modes

The crystal structure of tephroite (Online Materials[1] Fig. S2) represents conspicuous characteristics. The isolated SiO_4 tetrahedra have strong internal bonding but are distorted from the ideal T_d to C_s symmetry due to the static crystal-field forces and dynamic interaction between SiO_4 units. The bonding of Mn at M1 and M2 is much weaker than that in the SiO_4 tetrahedron. Therefore, the lattice vibrations of Mn cations and external SiO_4 occur at relatively low wavenumbers and are profoundly affected by the crystal-chemical environment in which they occur, while internal SiO_4 vibrations occur at high wavenumbers, between 800–1100 cm^{-1} (Stidham et al. 1976; Hofmeister 1987; Rao et al. 1988; Chopelas 1991; Kolesov and Geiger 2004).

The Raman spectra of tephroite are analogous to those of other end-member olivines. For example, the vibrational modes of tephroite are considered to systematically shift to frequencies 15–25 cm^{-1} lower than the corresponding bands of forsterite (Chopelas 1991; Liu and Mernagh 1993; Kolesov and Geiger 2004; Mouri and Enami 2008) but the corresponding vibrational frequencies of transition metal olivine $(Mn,Fe,Co,Ni)_2SiO_4$ are similar (Mouri and Enami 2008). In a broad sense, metal ions do not constitute an important factor controlling the relative motion of Raman-active vibrations. The approximation of the internal and external modes effectively describes these vibrations (Stidham et al. 1976). The discrepancies in Raman frequencies are caused by slightly different nonbonded atomic force constants due to lattice expansion or contraction when metal ions are replaced. The Raman spectrum of tephroite is complicated due to self-absorption (Stidham et al. 1976). More than half of the low-frequency lattice vibrations seen for forsterite and natural olivine cannot be observed in this study.

The ν_3 mode at 934 cm^{-1} shows the greatest pressure dependence of the high-frequency Ag modes of SiO_4 tetrahedra (Fig. 3), which is similar to previous studies (Chopelas 1991; Hushur et al. 2009; Liu et al. 2021). A previous study pointed out that there is a net force on Si toward O1 due to Coulomb repulsion between Si and three metallic atoms, resulting in the Si-O1 bond (1.62 Å) being shorter than other Si-O bonds (1.64 and 1.67 Å). Moreover, ν_3 becomes more sensitive to the volume of the M1 and M2 octahedra (Lam et al. 1990).

The mode Grüneisen parameters of the internal vibrational modes (ν_4, ν_1, and ν_3) range from 0.3 to 0.62 in the frequency range above 500 cm^{-1} and are systematically smaller than the mode Grüneisen parameters of 1.02–1.64 in lower-frequency lattice vibrations (Online Materials[1] Table S7). The translation of the isolated SiO_4 and metallic cations is more sensitive to changes in pressure, while the Si-O bonds reflect their strong

bond energy and incompressibility inside the SiO_4 tetrahedra. The volume changes mainly depend on the weak bonds in the crystal structure, and the low-frequency modes associated with the weak bands are more susceptible to pressure-induced volume changes. The mode Grüneisen parameters obtained from the pressure shift of the modes are closely related. This sheds light on the compression mechanism of tephroite controlled by compression of the voids and MnO_6 octahedra rather than SiO_4 tetrahedra, which is consistent with the results derived from the SCXRD structural refinement.

Amorphous phenomena have also been observed in previous high-pressure Raman experiments on other end-member olivines. Durben et al. (1993) observed two new Raman bands, a relatively strong band near 825 cm^{-1} and a weaker band at ~1060 cm^{-1}, above 30 GPa in forsterite. The extrapolated ambient positions of the two new bands are 750 and 960 cm^{-1}. It is supposed that forsterite does not experience an olivine-to-spinel conversion, but the spectral changes are a prelude to amorphization at higher pressures. On decompression, forsterite returns to its initial frequencies during the recovery of the sample under ambient conditions (Durben et al. 1993; Santamaria-Perez et al. 2016; Williams et al. 1989). In this study, after the amorphization of tephroite, the SiO_4 tetrahedra may collapse, but the amorphous-like phase still has a partially ordered structure, so there will be peaks near 250 and 640 cm^{-1}. When the pressure is relieved, tephroite tries to restore its original structure like other end-member olivines (Durben et al. 1993; Rouquette et al. 2008; Santamaria-Perez et al. 2016), and the characteristic Raman peaks of olivine at 800–840 cm^{-1} appear. However, due to the collapse of the structure caused by the amorphization of tephroite, it is difficult to restore its initial olivine structure after depressurization, and only the enhancement of the peak near 830–840 cm^{-1} is seen. A new peak near 750 cm^{-1} in the frequency range of typical symmetric stretching vibrations of Si-O-Si dimer linkages is observed in pyrosilicate structures and β-Mg_2SiO_4 (Piriou and McMillan 1983; McMillan and Akaogi 1987). The formation of high-coordinate Si polyhedral species or Si-O-Si linkages formed in Si_2O_7 dimer defects is given as the reason for the emergence of the band at 750 cm^{-1} (Williams et al. 1989). Similar peaks also appear at frequencies of 820–840 cm^{-1} above 40 GPa for $(Mg_{0.9}Fe_{0.1})_2SiO_4$ that are also considered to be associated with Si-O-Si linkages between pressure-induced dimerization adjacent to SiO_4 tetrahedra that result in fivefold- or sixfold-coordinated silicate species (Rouquette et al. 2008; Santamaria-Perez et al. 2016).

Additionally, four new Raman bands are detected in Ni-olivine under non-hydrostatic compression above 30 GPa, and the vibration frequencies extrapolated to zero pressure are 944, 843, 737, and 235 cm^{-1} (Lin 2001). The new bands corresponding to ν_0 at 235 and 737 cm^{-1} are close to the ν_0 found at 215 and 748 cm^{-1} for tephroite in this study, but ν_0 at 235 and 843 cm^{-1} is not observed in forsterite. It is suggested that the appearance of these new bands may indicate the formation of a new high-pressure phase, and it may also imply that irreversible amorphization of Ni-olivine occurs at higher pressure (P > 40 GPa). However, the variation in the Raman bands of tephroite is different from those of forsterite and Ni-olivine. A distinct characteristic is the disappearance of the prominent vibrational frequencies of $\nu_1+\nu_3$ at 809 and 841 cm^{-1} as new bands appear in the Raman spectra of tephroite at 21 GPa. It indicates that the SiO_4 tetrahedra may collapse, but the amorphous-like phase of tephroite still has a partially ordered structure. If the pressure is increased beyond the stability field of the structure, the olivine atomic configurations are frozen and accompanied by atomic rearrangement due to saturation of the compression mechanism (Machon et al. 2014).

Amorphous transformation pressure of tephroite: The lowest pressure in end-member olivines

Tephroite undergoes PIA, as observed in both high-pressure SCXRD and Raman scattering experiments in this study. Similar observations have been obtained in other end-member components of olivine in previous studies.

Partial amorphization of natural peridot $(Mg_{0.88}Fe_{0.12})_2SiO_4$ was first observed in a single crystal shock-wave experiment at ~56 GPa (Jeanloz et al. 1977). Fayalite glass with olivine and spinel phases was first found in laser-heated diamond-anvil cell (LHDAC) experiments and was similar to that found in shocked chondritic meteorites (Lacam et al. 1980). Guyot and Reynard (1992) experimented with San Carlos olivine powder crystalline samples under high-P-T experiments in a LHDAC. The recovered samples were mainly amorphous when the temperature was lower than 700 °C, and the maximum pressure was >70 GPa. However, the recovered samples from lower pressure (30–70 GPa) displayed a partial amorphous character and were accompanied by a hexagonally close-packed lattice (Guyot and Reynard 1992).

Raman spectroscopic investigation of forsterite showed that all sharp crystalline peaks disappeared at ~54 GPa, indicating this was the pressure of complete PIA (Santamaria-Perez et al. 2016). Recently, Kim et al. (2021) examined polycrystalline and single-crystal forsterite by in situ XRD measurements in laser-shocked experiments. Their results showed that the polycrystalline crystals underwent amorphization above 79 GPa, while the complete amorphous transformation of the oriented crystals occurred under higher pressure. It is worth noting that forsterite was shown to transform into an amorphous state upon decompression to ambient pressure after undergoing a high-pressure metastable transformation to forsterite III (Finkelstein et al. 2014). In contrast to the high-amorphous transformation pressure of forsterite, fayalite becomes amorphous at ~40 GPa. Williams et al. (1990) observed the irreversible amorphous transformation of fayalite upon compression to 42 GPa by infrared spectroscopic measurements, which is believed to be associated with an increase in the coordination of silicon. Additionally, first-principles molecular dynamics simulations supported the amorphization of fayalite at 40 GPa (Misawa and Shimojo 2020), and not only sixfold- but also fivefold- coordinated silicon atoms were present in the amorphized structure under high pressures.

However, the amorphization pressure is significantly decreased without the use of any pressure-transmitting medium. Under these circumstances, the appearance of amorphous features in forsterite only occurs between 30–40 GPa (Durben et al. 1993; Andrault et al. 1995; Rouquette et al. 2008). In particular, for fayalite, the pressure for the appearance of amorphization is only 12 GPa (Andrault et al. 1995). Andrault et al. (1995) conducted in situ energy-dispersive XRD for forsterite-fayalite solid solutions. They claimed that although a wide range of

amorphous features was observed at increasing pressure as the forsterite content increased, the samples still exhibited some crystalline diffraction at the highest pressures (25–59 GPa). It is worth noting that the results of Richard and Richet (1990) showed that the amorphization pressure of fayalite under non-hydrostatic conditions is similar to that in hydrostatic experiments. Additionally, new Raman bands were observed in Ni-olivine under non-hydrostatic compression above 30 GPa, suggesting that amorphization may occur at higher pressures (>40 GPa) (Lin 2001). However, Ni-olivine still maintained its initial structure, and no phase transition was observed in a high-pressure SCXRD experiment up to 42.5 GPa (Zhang et al. 2019).

Combined with the results of the amorphization of tephroite in this study, it is evident that the amorphization pressure of olivine decreases with increasing metallic cation radius (Fig. 5). Tephroite, with the largest metallic cation radius, shows the lowest pressure for amorphous transformation. Different from other end-member olivines, the tephroite rapidly undergoes amorphous transformation without the original characteristics of olivine crystal. Moreover, the Raman spectra of tephroite do not return to their initial state upon decompression to ambient pressure. Compared with previous results (Durben et al. 1993; Rouquette et al. 2008; Santamaria-Perez et al. 2016), the two primary Raman peaks related to the Si-O stretching mode (ν_1 and ν_3) reappear during the decompression process, which means the tetrahedrally bonded silicate units are restored. But this phenomenon does not appear in this paper (Fig. 3). Previous studies have also observed that the PIA of some materials [e.g., berlinite ($AlPO_4$)] returns to the initial crystalline orientation during the recovery process, the so-called memory glass effect (Meade and Jeanloz 1991). Later work showed that there is no amorphization but a distorted metastable crystalline phase, which has been proven to be a high-density crystalline phase (Gillet et al. 1995; Pellicer-Porres et al. 2007).

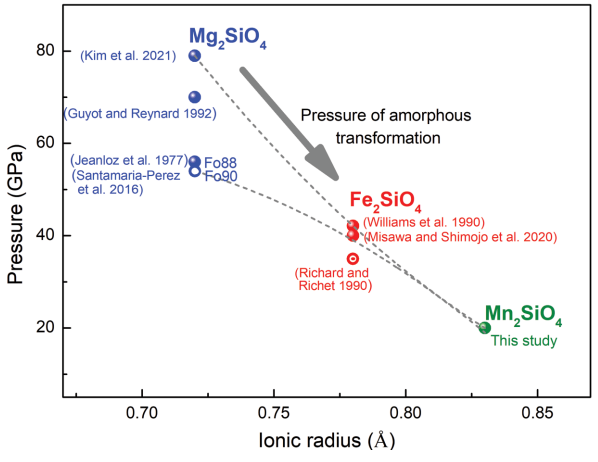

Figure 5. Amorphous transformation pressure of end-member olivine $(Mg,Fe,Mn)_2SiO_4$ with ionic radius. The amorphization pressure of olivine from previous studies is shown for comparison (Jeanloz et al. 1977; Williams et al. 1990; Richard and Richet 1990; Guyot and Reynard 1992; Santamaria-Perez et al. 2016; Misawa and Shimojo 2020; Kim et al. 2021). The solid circles indicate a mixture of crystalline and amorphous phases, hollow circles represent the complete amorphous pressure, and the points inside the hollow circles represent the pressure at which the samples are partially amorphous. The gray dashed curves represent the polynomial fits. (Color online.)

The type of the sample (single crystal or powder), impurities, compression rate, and temperature are factors that lead to the amorphous transformation. (Kingma et al. 1993; Ekbundit et al. 1996; Machon et al. 2014). No system can be compressed infinitely, which eventually leads to structural collapse. When structural collapse occurs at a low temperature or on a rapid timescale, ionic or atomic diffusion or bond rearrangement does not occur, resulting in a new crystalline lattice that is an amorphous solid. Amorphous material can also be formed under non-hydrostatic conditions. If the material leaves the metastable extension of its free energy curve under lower pressure and there is not sufficient thermal energy to achieve metastable crystals, the process of amorphization occurs (Machon et al. 2014; Santamaria-Perez et al. 2016). Rouquette et al. (2008) explained that the spin transition of iron leads to the amorphization of olivine in the 50 to 75 GPa range through high-pressure Mössbauer data at room temperature. The substitution of iron for magnesium in the olivine structure decreases the pressure required for saturation of the structural compression. Therefore, the reduction in the iron ionic radius [$r_{Fe^{2+}}$(HS) = 78 pm and $r_{Fe^{2+}}$(LS) = 61 pm] after spin transition causes a local collapse of the structure, resulting in a downshift in the pressure of the amorphous transition. This phenomenon is in contrast to the results of this study in that the amorphization pressure decreases with increasing ionic radius. The larger Mn ionic radius results in a lower amorphous transition pressure. The amorphization pressures of forsterite, fayalite, and tephroite show a downward trend with increasing metal ion radius. Therefore, Ni-olivine transforms into an amorphous state under higher pressure than forsterite. The substitution of iron or Mn ions for magnesium ions may reduce the local energetic barriers and further affect the structural transformation kinetics (Santamaria-Perez et al. 2016).

Geophysical Implications

The Mn-rich mineral inclusions found in ophiolite-host diamonds are speculated to have originated at a depth of 200–250 km and to be related to the early subducted normal mid-ocean ridge basalts (MORB) with a 10% ferromanganese crustal composition. These Mn-rich minerals included in diamonds are mainly Ni-Mn-Co alloys, Mn silicate (e.g., Mn, Ca silicate with an orthorhombic perovskite structure, tephroite, and spessartine), and MnO (Robinson et al. 2015; Moe et al. 2018; Lian et al. 2018; Lian and Yang 2019; Wu et al. 2019). A proportion of Mn-nodules and Mn-bearing sediments are distributed at the bottom of the ocean (Verlaan et al. 2004), which are in the subducted slab before the formation of the ophiolite.

The SCXRD and Raman spectroscopy experiments in this study confirm that tephroite undergoes an amorphous transformation at ~900 K and ~20 GPa (Fig. 6a). The amorphous phase cannot return to the original olivine structure after cooling and depressurization. Moreover, unlike forsterite and fayalite, a previous study observed that tephroite decomposed into MnO plus $MnSiO_3$ at ~14 GPa and ~1273 K and further decomposed into MnO plus SiO_2 at ~30 GPa (Ito et al. 1974). Mn-nodules are thought to be distributed at the bottom of the oceanic crust

(Verlaan et al. 2004), and the high density of tephroite promotes the subduction of the slab into Earth's interior. There is a situation when an ancient oceanic slab with lower temperatures subducts rapidly [e.g., Tonga slab with a center temperature of 800 K to 600 km (Bina and Navrotsky 2000; Ganguly et al. 2009)], amorphous tephroite would appear as the slab subducts into the transition zone and even deeper. In addition, amorphous olivine may cause grain boundary flow, which enhances sliding and causes a significant decrease in viscosity (Samae et al. 2021). The low viscosity of amorphous tephroite and metastable olivine and pyroxene (Xu et al. 2020b) may be the possible factors resulting in the stagnation of the cold slab in the transition zone. Therefore, tephroite may exist in stagnant slabs as an amorphous phase. However, for the subducting slab with higher temperature, tephroite may be decomposed into MnO and $MnSiO_3$ under high pressure and high temperature and even continue to decompose into MnO and SiO_2.

Ample evidence suggests that crustal materials subducted into the deep Earth can be brought back to the surface through mantle convection or mantle plumes (Xiong et al. 2015; Yang et al. 2015b). Figure 17 in Yang et al. (2015a) shows that tephroite is surrounded by MnO, Mn-garnet, and $(Ni,Co)_3Mn$ in ophiolite-hosted diamonds. There may be a situation where the low-viscosity amorphous tephroite is more likely to be wrapped in the alloy melt (Fig. 6). During rapid uplift (Howell et al. 2015; McGowan et al. 2015), the carbon in the alloy melt is quickly exsolved as diamond (Sokol et al. 2009). Under the impact of high temperature, the diamond grows, and the amorphous tephroite recrystallizes and further decomposes into MnO and Mn-garnet. The resulting products then encased the recrystallized tephroite. In another possible situation, the amorphous tephroite crystallized under the influence of high temperature before being wrapped by a diamond and further decomposed during transportation. Therefore, the state of tephroite at higher temperatures needs to be constrained by more experiments. Mixtures of UHP, highly reduced minerals, and crustal materials coexist in ophiolitic peridotites and chromitites far from their normal stability fields (Robinson et al. 2015; Yang et al. 2015a, 2015b), indicating that their formation is multistage and that UHP and highly reduced minerals are formed in the deep mantle.

The mineral inclusions in diamonds provide a good window for understanding the deep cycling of oceanic crustal materials and the composition of the deep mantle. Tephroite can exist in an amorphous form in a stagnant slab at the transition zone and even in the lower mantle. Amorphous tephroite or some other amorphous substances would profoundly influence the distribution of elements, transparency properties, and kinetic properties in the Earth's interior. Further works are of vital importance to discussing the amorphous phase in the system and may be able to elucidate deep crustal material recycling.

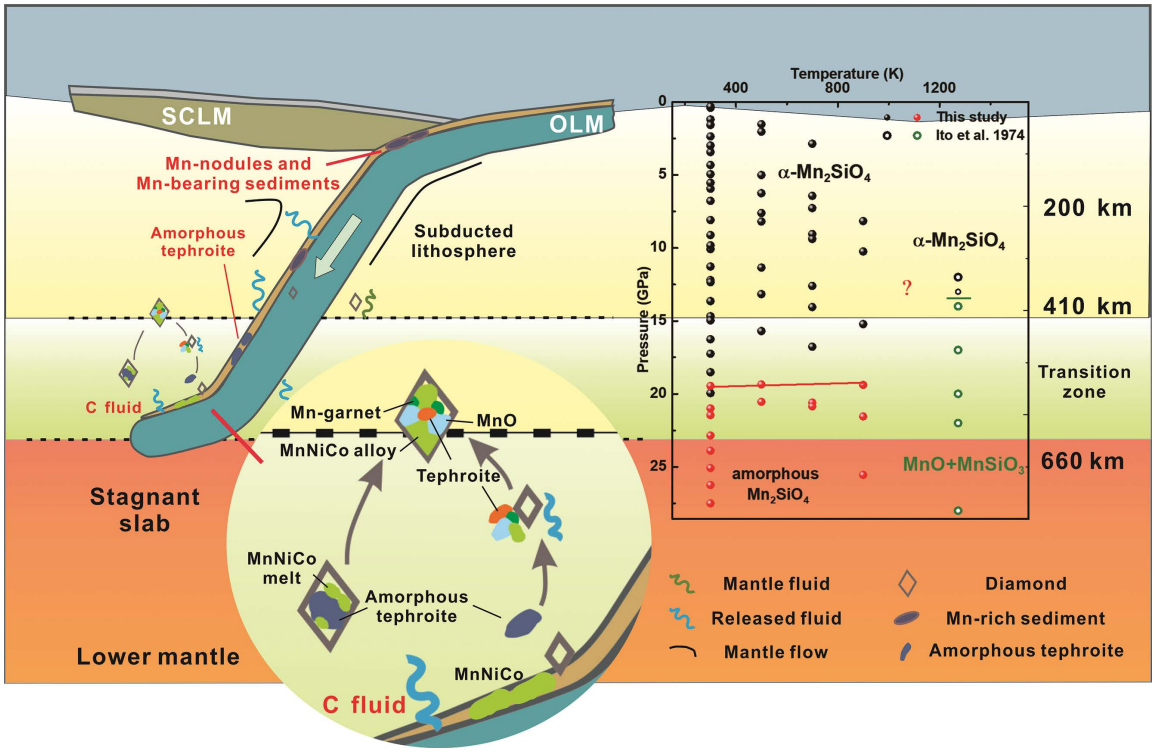

Figure 6. Schematic graph of diamond formation with tephroite. Subduction brings the Mn-bearing oceanic crustal assemblage into the Earth's interior. The slab subducts to the transition zone with a partially metal alloy melt, which further evolves into a MnNiCo alloy melt. The buoyant material returns to shallow depths during rapid uplift. In the process of the uplift and growth of diamonds, some of the alloy melt and some of the high-density materials are included. Phase diagram of tephroite under high-*P-T* conditions. The black and red solid circles represent α-tephroite and amorphous tephroite in this study, respectively. The black and green hollow points are α-tephroite and decomposition products of MnO and $MnSiO_3$ (tetragonal garnet), respectively. (Color online.)

Data availability

All data generated or analyzed during this study are included in this published article and its Online Materials[1] files.

Acknowledgments

We acknowledge Sergey N. Tkachev and Bin Yang for gas loading assistances. The authors declare no competing financial interests. Z.Y., J.X., and D.F. designed the project. Z.Y., J.X., D.F., D.Z., W.Z., and H.X. participated in the data collection and analysis. Z.Y. and J.X. were responsible for data interpretation and wrote the manuscript. D.F., D.Z., W.Z., and H.X. participated in the discussion and provided comments on the manuscript.

Funding

This project was funded by the National Natural Science Foundation of China (Nos. 42172048 and U2032118), Guizhou Provincial Science and Technology Projects (QKHPTRCYQK[2023]035 and QKHJC-ZK[2021]ZD042), Hundred Talents Program of the Chinese Academy of Sciences, and Guizhou Provincial 2020 and 2021 Science and Technology Subsidies (Nos. GZ2020SIG and GZ2021SIG). The experiments were performed at GeoSoilEnviroCARS (13-BM-C), Advanced Photon Source (APS), and Argonne National Laboratory. The use of the gas-loading system is supported by COMPRES and GeoSoilEnviroCARS. GeoSoilEnviroCARS is supported by the National Science Foundation–Earth Sciences (EAR-1634415) and the Department of Energy–Geosciences (DE-FG02-94ER14466). COMPRES is under NSF Cooperative Agreement EAR-1661511. Use of the Advanced Photon Source was supported by the U.S. Department of Energy, Office of Science, Office of Basic Energy Sciences, under Contract No. DE-AC02-06CH11357.

References cited

Andrault, D., Bouhifd, M.A., Itié, J.P., and Richet, P. (1995) Compression and amorphization of $(Mg,Fe)_2SiO_4$ olivines: An X-ray diffraction study up to 70 GPa. Physics and Chemistry of Minerals, 22, 99–107, https://doi.org/10.1007/BF00202469.

Angel, R.J., Alvaro, M., and Gonzalez-Platas, J. (2014) EosFit7c and a Fortran module (library) for equation of state calculations. Zeitschrift für Kristallographie. Crystalline Materials, 229, 405–419, https://doi.org/10.1515/zkri-2013-1711.

Bina, C.R. and Navrotsky, A. (2000) Possible presence of high-pressure ice in cold subducting slabs. Nature, 408, 844–847, https://doi.org/10.1038/35048555.

Birch, F. (1947) Finite elastic strain of cubic crystals. Physical Review, 71, 809–824, https://doi.org/10.1103/PhysRev.71.809.

Chopelas, A. (1991) Single crystal Raman spectra of forsterite, fayalite, and monticellite. American Mineralogist, 76, 1101–1109.

Cloutis, E.A. (1997) Manganese-rich olivines: Identification from spectral reflectance properties. Journal of Geophysical Research, 102 (E11), 25575–25580, https://doi.org/10.1029/97JE02497.

Dolomanov, O.V., Bourhis, L.J., Gildea, R.J., Howard, J.A.K., and Puschmann, H. (2009) OLEX2: A complete structure solution, refinement and analysis program. Journal of Applied Crystallography, 42, 339–341, https://doi.org/10.1107/S0021889808042726.

Downs, R.T., Zha, C.-S., Duffy, T.S., and Finger, L.W. (1996) The equation of state of forsterite to 17.2 GPa and effects of pressure media. American Mineralogist, 81, 51–55.

Durben, D.J., McMillan, P.F., and Wolf, G.H. (1993) Raman study of the high-pressure behavior of forsterite (Mg_2SiO_4) crystal and glass. American Mineralogist, 78, 1143–1148.

Ekbundit, S., Leinenweber, K., Yarger, J.L., Robinson, J.S., Verhelst-Voorhees, M., and Wolf, G.H. (1996) New high-pressure phase and pressure-induced amorphization of $Ca(OH)_2$: Grain size effect. Journal of Solid State Chemistry, 126, 300–307, https://doi.org/10.1006/jssc.1996.0341.

Fei, Y. (1995) Thermal expansion. In T.J. Ahrens, Ed., Mineral Physics & Crystallography: A Handbook of Physical Constants pp. 29–44, American Geophysical Union.

Fei, Y., Ricolleau, A., Frank, M., Mibe, K., Shen, G., and Prakapenka, V. (2007) Toward an internally consistent pressure scale. Proceedings of the National Academy of Sciences, 104, 9182–9186, https://doi.org/10.1073/pnas.0609013104.

Finkelstein, G.J., Dera, P.K., Jahn, S., Oganov, A.R., Holl, C.M., Meng, Y., and Duffy, T.S. (2014) Phase transitions and equation of state of forsterite to 90 GPa from single-crystal X-ray diffraction and molecular modeling. American Mineralogist, 99, 35–43, https://doi.org/10.2138/am.2014.4526.

Frost, D.J. (2008) The upper mantle and transition zone. Elements, 4, 171–176, https://doi.org/10.2113/GSELEMENTS.4.3.171.

Fujino, K., Sasaki, S., Takéuchi, Y., and Sadanaga, R. (1981) X-ray determination of electron distributions in forsterite, fayalite and tephroite. Acta Crystallographica, B37, 513–518, https://doi.org/10.1107/S0567740881003506.

Gaillard, F., Scaillet, B., Pichavant, M., and Iacono-Marziano, G. (2015) The redox geodynamics linking basalts and their mantle sources through space and time. Chemical Geology, 418, 217–233, https://doi.org/10.1016/j.chemgeo.2015.07.030.

Ganguly, J., Freed, A.M., and Saxena, S.K. (2009) Density profiles of oceanic slabs and surrounding mantle: Integrated thermodynamic and thermal modeling, and implications for the fate of slabs at the 660 km discontinuity. Physics of the Earth and Planetary Interiors, 172, 257–267, https://doi.org/10.1016/j.pepi.2008.10.005.

Geiger, C.A., Grodzicki, M., and Dachs, E. (2019) An analysis of the magnetic behavior of olivine and garnet substitutional solid solutions. American Mineralogist, 104, 1246–1255, https://doi.org/10.2138/am-2019-6839CCBYNCND.

Gillet, P. and Guyot, F. (1988) High pressure-high temperature Raman spectroscopy of Ca_2GeO_4 (olivine form): Some insights on anharmonicity. Chemical Geology, 70, 61, https://doi.org/10.1016/0009-2541(88)90362-2.

Gillet, P., Badro, J., Varrel, B., and McMillan, P.F. (1995) High-pressure behavior in α-$AlPO_4$: Amorphization and the memory-glass effect. Physical Review B: Condensed Matter, 51, 11262–11269, https://doi.org/10.1103/PhysRevB.51.11262.

Guyot, F. and Reynard, B. (1992) Pressure-induced structural modifications and amorphization in olivine compounds. Chemical Geology, 96, 411–420, https://doi.org/10.1016/0009-2541(92)90069-H.

Hofmeister, A.M. (1987) Single-crystal absorption and reflection infrared spectroscopy of forsterite and fayalite. Physics and Chemistry of Minerals, 14, 499–513, https://doi.org/10.1007/BF00308285.

Howell, D., Griffin, W.L., Yang, J., Gain, S., Stern, R.A., Huang, J.-X., Jacob, D.E., Xu, X., Stokes, A.J., O'Reilly, S.Y., and others. (2015) Diamonds in ophiolites: Contamination or a new diamond growth environment? Earth and Planetary Science Letters, 430, 284–295, https://doi.org/10.1016/j.epsl.2015.08.023.

Hushur, A., Manghnani, M.H., Smyth, J.R., Nestola, F., and Frost, D.J. (2009) Crystal chemistry of hydrous forsterite and its vibrational properties up to 41 GPa. American Mineralogist, 94, 751–760, https://doi.org/10.2138/am.2009.2990.

Ito, E., Matsumoto, T., and Kawai, N. (1974) High-pressure decompositions in manganese silicates and their geophysical implications. Physics of the Earth and Planetary Interiors, 8, 241–245, https://doi.org/10.1016/0031-9201(74)90090-9.

Jeanloz, R., Ahrens, T.J., Lally, J.S., Nord, G.L. Jr., Christie, J.M., and Heuer, A.H. (1977) Shock-produced olivine glass: First observation. Science, 197, 457–459, https://doi.org/10.1126/science.197.4302.457.

Kim, D., Tracy, S.J., Smith, R.F., Gleason, A.E., Bolme, C.A., Prakapenka, V.B., Appel, K., Speziale, S., Wicks, J.K., Berryman, E.J., and others. (2021) Femtosecond X-ray diffraction of laser-shocked forsterite (Mg_2SiO_4) to 122 GPa. Journal of Geophysical Research, 126, 1–14, https://doi.org/10.1029/2020JB020337.

Kingma, K.J., Hemley, R.J., Mao, H., and Veblen, D.R. (1993) New high-pressure transformation in α -quartz. Physical Review Letters, 70, 3927–3930, https://doi.org/10.1103/PhysRevLett.70.3927.

Kolesov, B.A. and Geiger, C.A. (2004) A Raman spectroscopic study of Fe-Mg olivines. Physics and Chemistry of Minerals, 31, 142–154, https://doi.org/10.1007/s00269-003-0370-y.

Lacam, A., Madon, M., and Poirier, J.P. (1980) Olivine glass and spinel formed in a laser heated, diamond-anvil high pressure cell. Nature, 288, 155–157, https://doi.org/10.1038/288155a0.

Lam, P.K., Yu, R., Lee, M.W., and Sharma, S.K. (1990) Structural distortions and vibrational modes in Mg_2SiO_4. American Mineralogist, 75, 109–119.

Lian, D. and Yang, J. (2019) Ophiolite-hosted diamond: A new window for probing carbon cycling in the deep mantle. Engineering (Beijing), 5, 406–420, https://doi.org/10.1016/j.eng.2019.02.006.

Lian, D., Yang, J., Wiedenbeck, M., Dilek, Y., Rocholl, A., and Wu, W. (2018) Carbon and nitrogen isotope, and mineral inclusion studies on the diamonds from the Pozanti-Karsanti chromitite, Turkey. Contributions to Mineralogy and Petrology, 173, 72, https://doi.org/10.1007/s00410-018-1499-5.

Lin, C.C. (2001) High-pressure Raman spectroscopic study of Co- and Ni-olivines. Physics and Chemistry of Minerals, 28, 249–257, https://doi.org/10.1007/s002690100158.

Liu, L.-G. and Mernagh, T.P. (1993) Raman spectra of forsterite and fayalite at high pressures and room temperature. High Pressure Research, 11, 241–256, https://doi.org/10.1080/08957959308203152.

Liu, D., Guo, X., Smyth, J.R., Wang, X., Zhu, X., Miao, Y., Bai, J., and Ye, Y. (2021) High-temperature and high-pressure Raman spectra of $Fo_{89}Fa_{11}$ and $Fo_{58}Fa_{42}$ olivines: Iron effect on thermodynamic properties. American Mineralogist, 106, 1668–1678, https://doi.org/10.2138/am-2021-7686.

Machon, D., Meersman, F., Wilding, M.C., Wilson, M., and McMillan, P.F. (2014) Pressure-induced amorphization and polyamorphism: Inorganic and biochemical systems. Progress in Materials Science, 61, 216–282, https://doi.org/10.1016/j.pmatsci.2013.12.002.

Mao, H.K., Xu, J., and Bell, P.M. (1986) Calibration of the ruby pressure gauge to 800 kbar under quasi-hydrostatic conditions. Journal of Geophysical Research, 91 (B5), 4673, https://doi.org/10.1029/JB091iB05p04673.

Mason, B. (1963) Olivine composition in chondrites. Geochimica et Cosmochimica Acta, 27, 1011–1023, https://doi.org/10.1016/0016-7037(63)90062-0.

McGowan, N.M., Griffin, W.L., González-Jiménez, J.M., Belousova, E., Afonso, J.C., Shi, R., McCammon, C.A., Pearson, N.J., and O'Reilly, S.Y. (2015) Tibetan chromitites: Excavating the slab graveyard. Geology, 43, 179–182,

https://doi.org/10.1130/G36245.1.
McMillan, P. and Akaogi, M. (1987) Raman spectra of β-Mg_2SiO_4 (modified spinel) and γ-Mg_2SiO_4 (spinel). American Mineralogist, 72, 361–364.
Meade, C. and Jeanloz, R. (1991) Deep-focus earthquakes and recycling of water into the Earth's mantle. Science, 252, 68–72, https://doi.org/10.1126/science.252.5002.68.
Misawa, M., and Shimojo, F. (2020) First-Principles study of pressure-induced amorphization of Fe_2SiO_4 fayalite. Physica Status Solidi (b), 257, 2000173.
Moe, K.S., Yang, J.-S., Johnson, P., Xu, X., and Wang, W. (2018) Spectroscopic analysis of microdiamonds in ophiolitic chromitite and peridotite. Lithosphere, 10, 133–141, https://doi.org/10.1130/L603.1.
Momma, K. and Izumi, F. (2011) VESTA 3 for three-dimensional visualization of crystal, volumetric and morphology data. Journal of Applied Crystallography, 44, 1272–1276, https://doi.org/10.1107/S0021889811038970.
Mouri, T. and Enami, M. (2008) Raman spectroscopic study of olivine-group minerals. Journal of Mineralogical and Petrological Sciences, 103, 100–104, https://doi.org/10.2465/jmps.071015.
Mustard, J.F., Poulet, F., Gendrin, A., Bibring, J.-P., Langevin, Y., Gondet, B., Mangold, N., Bellucci, G., and Altieri, F. (2005) Olivine and pyroxene diversity in the crust of Mars. Science, 307, 1594–1597, https://doi.org/10.1126/science.1109098.
Nguyen, A.N. and Zinner, E. (2004) Discovery of ancient silicate stardust in a meteorite. Science, 303, 1496–1499, https://doi.org/10.1126/science.1094389.
Pellicer-Porres, J., Saitta, A.M., Polian, A., Itié, J.P., and Hanfland, M. (2007) Six-fold-coordinated phosphorus by oxygen in $AlPO_4$ quartz homeotype under high pressure. Nature Materials, 6, 698–702, https://doi.org/10.1038/nmat1966.
Piriou, B. and McMillan, P. (1983) The high-frequency vibrational spectra of vitreous and crystalline orthosilicates. American Mineralogist, 68, 426–443.
Poe, B.T., Romano, C., Nestola, F., and Smyth, J.R. (2010) Electrical conductivity anisotropy of dry and hydrous olivine at 8 GPa. Physics of the Earth and Planetary Interiors, 181, 103–111.
Rao, K.R., Chaplot, S.L., Choudhury, N., Ghose, S., Hastings, J.M., Corliss, L.M., and Price, D.L. (1988) Lattice dynamics and inelastic neutron scattering from forsterite, Mg_2SiO_4: Phonon dispersion relation, density of states and specific heat. Physics and Chemistry of Minerals, 16, 83–97, https://doi.org/10.1007/BF00201334.
Richard, G. and Richet, P. (1990) Room-temperature amorphlzation of fayalite and high-pressure properties of Fe_2SiO_4 liquid. Geophysical Research Letters, 17, 2093–2096, https://doi.org/10.1029/GL017i012p02093.
Ringwood, A.E. (1991) Phase transformations and their bearing on the constitution and dynamics of the mantle. Geochimica et Cosmochimica Acta, 55, 2083–2110, https://doi.org/10.1016/0016-7037(91)90090-R.
Rivers, M., Prakapenka, V., Kubo, A., Pullins, C., Holl, C., and Jacobsen, S. (2008) The COMPRES/GSECARS gas-loading system for diamond anvil cells at the Advanced Photon Source. High Pressure Research, 28, 273–292, https://doi.org/10.1080/08957950802333593.
Robinson, P.T., Trumbull, R.B., Schmitt, A., Yang, J.-S., Li, J.-W., Zhou, M.-F., Erzinger, J., Dare, S., and Xiong, F. (2015) The origin and significance of crustal minerals in ophiolitic chromitites and peridotites. Gondwana Research, 27, 486–506, https://doi.org/10.1016/j.gr.2014.06.003.
Rouquette, J., Kantor, I., McCammon, C.A., Dmitriev, V., and Dubrovinsky, L.S. (2008) High-pressure studies of $(Mg_{0.9}Fe_{0.1})_2SiO_4$ olivine using raman spectroscopy, X-ray diffraction, and mössbauer spectroscopy. Inorganic Chemistry, 47, 2668–2673, https://doi.org/10.1021/ic701983w.
Samae, V., Cordier, P., Demouchy, S., Bollinger, C., Gasc, J., Koizumi, S., Mussi, A., Schryvers, D., and Idrissi, H. (2021) Stress-induced amorphization triggers deformation in the lithospheric mantle. Nature, 591, 82–86, https://doi.org/10.1038/s41586-021-03238-3.
Santamaria-Perez, D., Thomson, A., Segura, A., Pellicer-Torres, J., Manjon, F.J., Cora, F., McColl, K., Wilson, M., Dobson, D., and McMillan, P.F. (2016) Metastable structural transformations and pressure-induced amorphization in natural $(Mg,Fe)_2SiO_4$ olivine under static compression: A Raman spectroscopic study. American Mineralogist, 101, 1642–1650, https://doi.org/10.2138/am-2016-5389CCBY.
Sheldrick, G.M. (2008) A short history of SHELX. Acta Crystallographica, A64, 112–122, https://doi.org/10.1107/S0108767307043930.
Sokol, A.G., Palyanova, G.A., Palyanov, Y.N., Tomilenko, A.A., and Melenevsky, V.N. (2009) Fluid regime and diamond formation in the reduced mantle: Experimental constraints. Geochimica et Cosmochimica Acta, 73, 5820–5834, https://doi.org/10.1016/j.gca.2009.06.010.
Speziale, S., Duffy, T.S., and Angel, R.J. (2004) Single-crystal elasticity of fayalite to 12 GPa. Journal of Geophysical Research: Solid Earth, 109, 1–15.
Stidham, H.D., Bates, J.B., and Finch, C.B. (1976) Vibrational spectra of synthetic single crystal tephroite, Mn_2SiO_4. Journal of Physical Chemistry, 80, 1226–1234, https://doi.org/10.1021/j100552a023.
Verlaan, P.A., Cronan, D.S., and Morgan, C.L. (2004) A comparative analysis of compositional variations in and between marine ferromanganese nodules and crusts in the South Pacific and their environmental controls. Progress in Oceanography, 63, 125–158, https://doi.org/10.1016/j.pocean.2004.11.001.
Williams, Q., McMillan, P., and Cooney, T. (1989) Vibrational spectra of olivine composition glasses: The Mg-Mn join. Physics and Chemistry of Minerals, 16, 352–359, https://doi.org/10.1007/BF00199555.
Williams, Q., Knittle, E., Reichlin, R., Martin, S., and Jeanloz, R. (1990) Structural and electronic properties of Fe_2SiO_4-fayalite at ultrahigh pressures: Amorphization and gap closure. Journal of Geophysical Research, 95 (B13), 21549–21563, https://doi.org/10.1029/JB095iB13p21549.
Wu, W., Yang, J., Wirth, R., Zheng, J., Lian, D., Qiu, T., and Milushi, I. (2019) Carbon and nitrogen isotopes and mineral inclusions in diamonds from chromitites of the Mirdita ophiolite (Albania) demonstrate recycling of oceanic crust into the mantle. American Mineralogist, 104, 485–500, https://doi.org/10.2138/am-2019-6751.
Xiong, F., Yang, J., Robinson, P.T., Xu, X., Liu, Z., Li, Y., Li, J., and Chen, S. (2015) Origin of podiform chromitite, a new model based on the Luobusa ophiolite, Tibet. Gondwana Research, 27, 525–542, https://doi.org/10.1016/j.gr.2014.04.008.
Xu, J., Fan, D., Zhang, D., Li, B., Zhou, W., and Dera, P.K. (2020a) Investigation of the crystal structure of a low water content hydrous olivine to 29.9 GPa: A high-pressure single-crystal X-ray diffraction study. American Mineralogist, 105, 1857–1865, https://doi.org/10.2138/am-2020-7444.
Xu, J., Fan, D., Zhang, D., Guo, X., Zhou, W., and Dera, P.K. (2020b) Phase transition of enstatite-ferrosilite solid solutions at high pressure and high temperature: Constraints on metastable orthopyroxene in cold subduction. Geophysical Research Letters, 47, 1–10, https://doi.org/10.1029/2020GL087363.
Yang, J., Robinson, P.T., and Dilek, Y. (2015a) Diamond-bearing ophiolites and their geological occurrence. Episodes, 38, 344–364, https://doi.org/10.18814/epiiugs/2015/v38i4/82430.
Yang, J., Meng, F., Xu, X., Robinson, P.T., Dilek, Y., Makeyev, A.B., Wirth, R., Wiedenbeck, M., and Cliff, J. (2015b) Diamonds, native elements and metal alloys from chromitites of the Ray-Iz ophiolite of the Polar Urals. Gondwana Research, 27, 459–485, https://doi.org/10.1016/j.gr.2014.07.004.
Ye, Z., Fan, D., Tang, Q., Xu, J., Zhang, D., and Zhou, W. (2021) Constraining the density evolution during destruction of the lithospheric mantle in the eastern North China Craton. Gondwana Research, 91, 18–30, https://doi.org/10.1016/j.gr.2020.12.001.
Zhang, L. (1998) Single crystal hydrostatic compression of $(Mg,Mn,Fe,Co)_2SiO_4$ olivines. Physics and Chemistry of Minerals, 25, 308–312.
Zhang, J.S., Hu, Y., Shelton, H., Kung, J., and Dera, P. (2017) Single-crystal X-ray diffraction study of Fe_2SiO_4 fayalite up to 31 GPa. Physics and Chemistry of Minerals, 44, 171–179, https://doi.org/10.1007/s00269-016-0846-1.
Zhang, D., Hu, Y., Xu, J., Downs, R.T., Hammer, J.E., and Dera, P.K. (2019) High-pressure behavior of liebenbergite: The most incompressible olivine-structured silicate. American Mineralogist, 104, 580–587, https://doi.org/10.2138/am-2019-6680.
Zolensky, M.E., Zega, T.J., Yano, H., Wirick, S., Westphal, A.J., Weisberg, M.K., Weber, I., Warren, J.L., Velbel, M.A., Tsuchiyama, A., and others. (2006) Mineralogy and petrology of comet 81P/Wild 2 nucleus samples. Science, 314, 1735–1739, https://doi.org/10.1126/science.1135842.

Manuscript received May 22, 2022
Manuscript accepted December 7, 2022
Accepted manuscript online December 15, 2022
Manuscript handled by Ryosuke Sinmyo

Endnote:

[1]Deposit item AM-23-118606. Online Materials are free to all readers. Go online, via the table of contents or article view, and find the tab or link for supplemental materials. The CIF has been peer-reviewed by our Technical Editors.